Supplemental Material for: Structure of High-Pressure Supercooled and Glassy Water

Riccardo Foffi and Francesco Sciortino

Department of Physics, Sapienza Università di Roma,

Piazzale Aldo Moro, 2, 00185 Rome, Italy

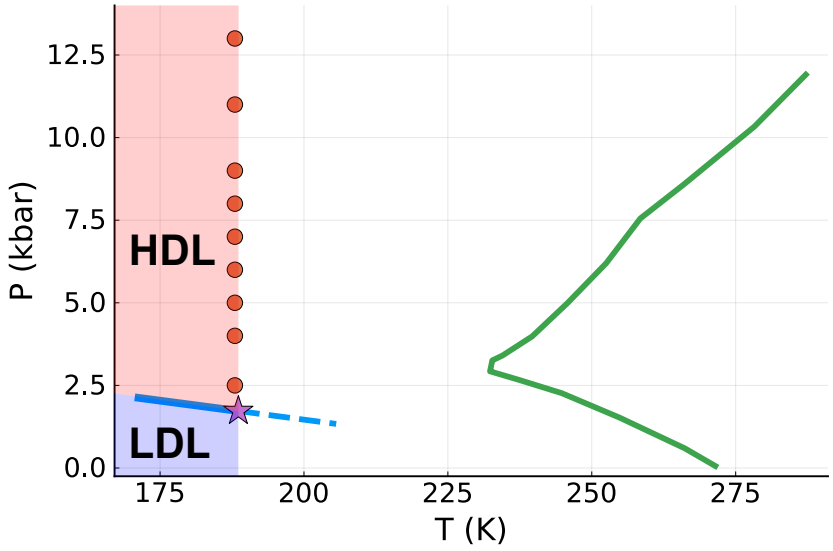

FIG. S1. P–T projection of the phase diagram of TIP4P/Ice, showing the explored state points (orange circles), the liquid-liquid critical point location estimated in Ref. [7] (violet star), the liquid-liquid transition line from Ref. [8] (solid blue line) and its extension in the supercritical regime (dashed blue line) and the solid-liquid coexistence curve from Ref. [1] (solid green line).

TABLE S1. Equilibration and production times of the MD simulations.

pressure / kbar	equilibration time / µs	production time / µs
2.5	5.0	5.0
4.0	6.0	6.5
5.0	13.0	12.0
6.0	7.0	8.0
7.0	15.5	12.0
8.0	13.0	10.0
9.0	15.0	12.0
11.0	14.0	12.0
13.0	14.0	12.0

DESCRIPTION OF THE SIMULATIONS

This study is based on a set of classical molecular dynamics (MD) simulations of $N = 1000$ water molecules interacting via the TIP4P/Ice potential [1] in the NPT ensemble, using

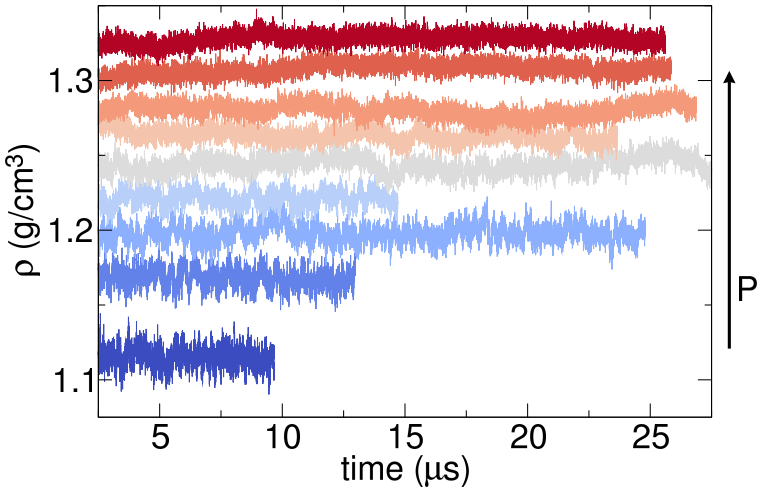

FIG. S2. Evolution of density in time along the 188 K isotherm. Colors from blue to red indicate increasing pressure from 2.5 to 13 kbar. The precise pressure values are listed in Table I.

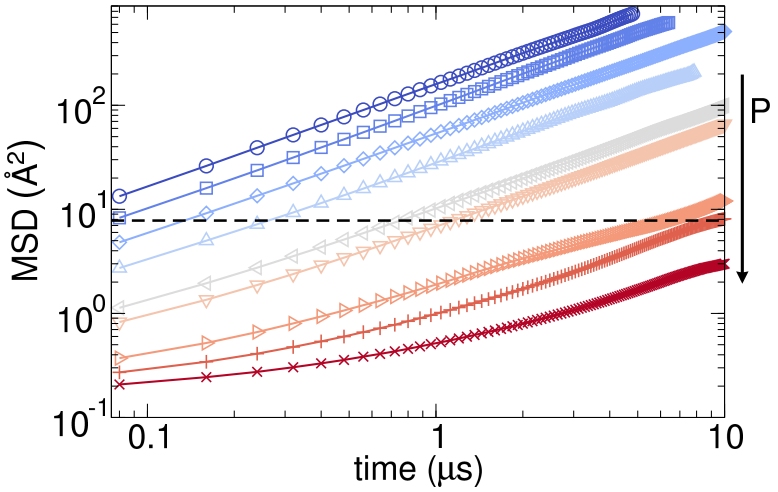

FIG. S3. Mean-square displacement of water molecules during the production phase of the MD simulations along the 188 K isotherm. Colors from blue to red indicate increasing pressure from 2.5 to 13 kbar. The precise pressure values are listed in Table I. The black dashed line at 7.8 Å^2 represents the nearest-neighbour distance squared.

GROMACS 5.1.4 [2] in single precision. A cubic simulation box with periodic boundary conditions was adopted. We chose a leap-frog integrator with a timestep of 2 fs. Temperature coupling was controlled via a Nosé-Hoover thermostat [3] with a characteristic time of 8 ps, and pressure coupling was controlled via an isotropic Parrinello-Rahman barostat [4]

with characteristic time 18 ps. Molecular constraints were implemented via the LINCS algorithm [5] at the sixth order, and van der Waals forces have been evaluated with a cutoff distance of 0.9 nm. To account for electrostatic interactions the particle-mesh Ewald method at the fourth order, with real-space cutoff 0.9 nm [6] was selected.

In Fig. S1 we show the location of the state points explored in this work, with respect to other relevant features of the phase diagram of the TIP4P/Ice model. Equilibration and production times for these state points are reported in Table S1. The simulations at pressures 2.5 and 4 kbar have been reproduced from Ref. [8], but the latter has been significantly extended. The evolution of density with time throughout the whole simulation is shown in Fig. S2; also, the molecular mean square displacements during the production phase are reported in Fig. S3. Apart from the highest density (associated to pressure 13 kbar), molecules have diffused, on average, a distance larger than the nearest neighbour distance (the hydrogen bond length, $r \approx 2.8\,\text{Å}$) during the production phase.

INHERENT STRUCTURES

We evaluated the inherent structures (IS) [9] by minimizing the potential energy via the steepest descent algorithm (STEEP) in GROMACS with a force tolerance of $1\,\text{J mol}^{-1}\,\text{nm}^{-1}$ and a maximum step size 5×10^{-4} nm. To ensure maximum accuracy, the minimization was carried in double precision. An example of the effect of the energy minimization on the liquid structure is shown in Fig. S4, for $P = 9$ kbar. The increase in short-range order causes a significant increase in the height of the first peak, enhancing the separation between the first and second hydration shells. In the intermediate range, only minor differences are observed, related to a slight enhancement of peaks and valleys, while the long-range correlations are practically unaffected.

In Fig. S5 we also show the complete pressure dependence of the $g(r)$ in the real dynamics, to be compared with Fig. 2 in main text. It is evident that the process of energy minimization enchances the structural features of the system without artificially altering them.

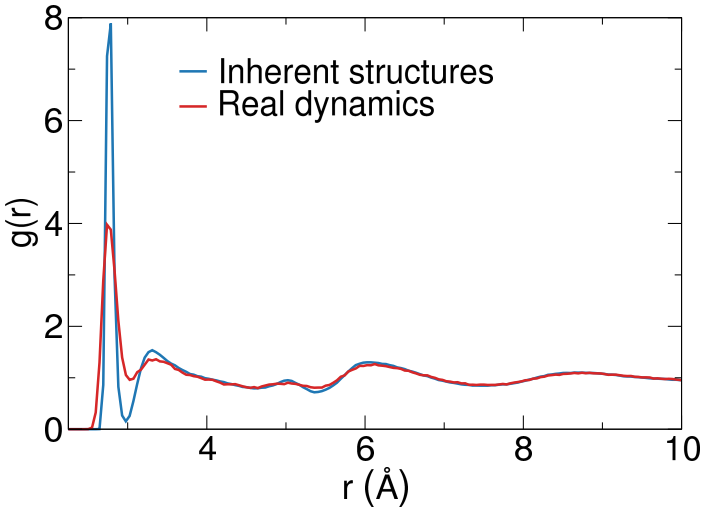

FIG. S4. Comparison of the radial distribution function of the liquid state ($T = 188\,\mathrm{K}$, $P = 9\,\mathrm{kbar}$) in the real dynamics and its inherent structures.

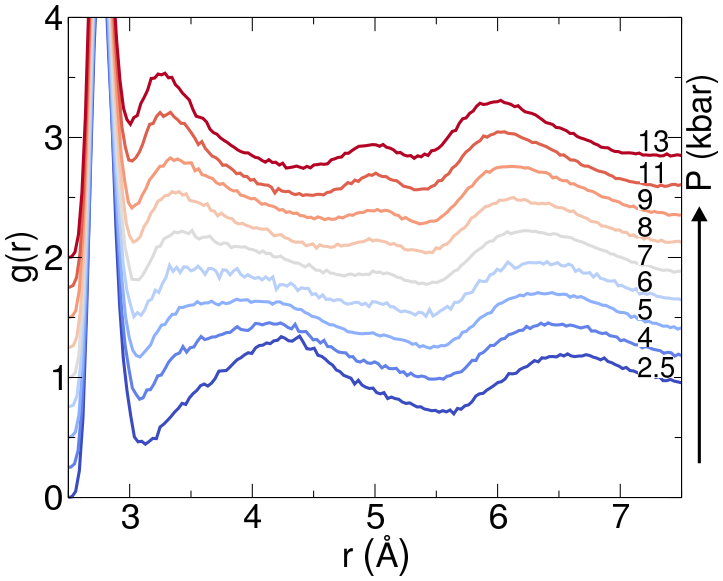

FIG. S5. Pressure dependence of the oxygen-oxygen $g(r)$ evaluated in the real dynamics along the 188 K isotherm. Successive $g(r)$ curves are shifted by 0.25 along the verical axis.

STRUCTURE FACTOR

The structural description provided by the radial distribution function (Fig. 2 in main text) is here complimented by its Fourier transform, the structure factor $S(q)$ [10], reported in Fig. S6 (evaluated in the IS). In Fig. S7 $S(q)$ is evaluated in the real dynamics, and

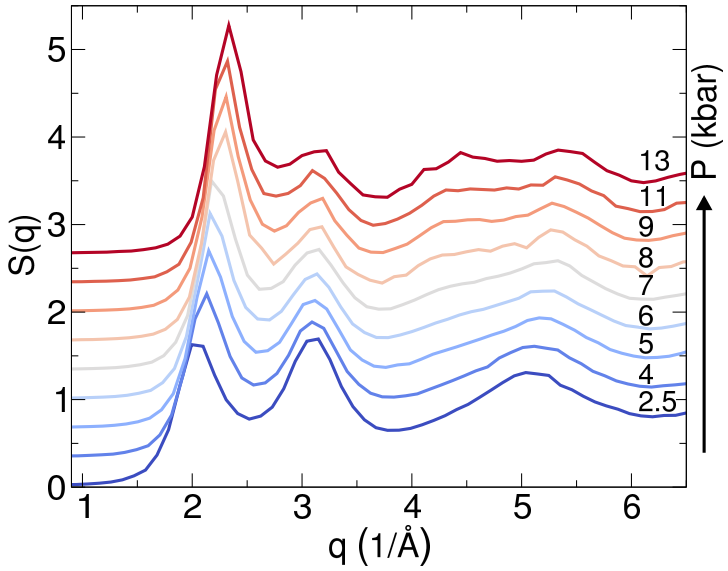

FIG. S6. Pressure dependence of the oxygen-oxygen structure factor evaluated in the IS along the 188 K isotherm. Successive $S(q)$ curves have been shifted by 1/3 along the vertical axis.

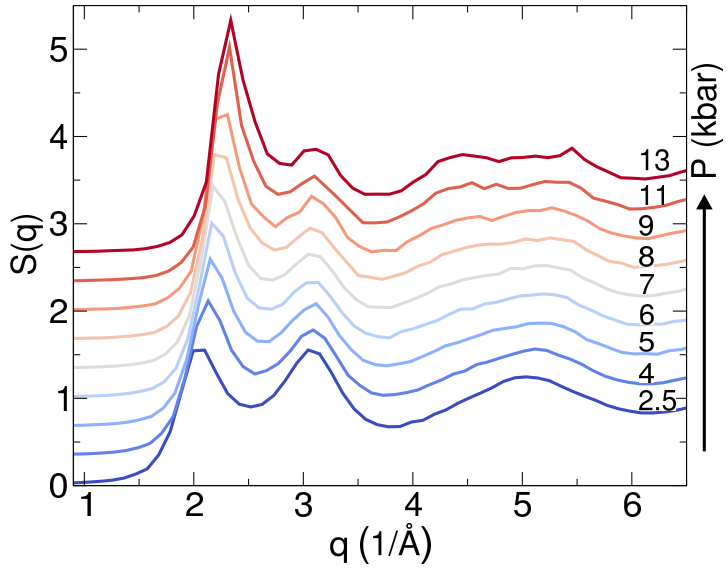

FIG. S7. Pressure dependence of the oxygen-oxygen structure factor evaluated in the real dynamics along the 188 K isotherm. Successive $S(q)$ curves have been shifted by 1/3 along the vertical axis.

once again we observe that the structural features of the system are not altered by energy minimization. In Fourier space one observes a clear shift (and enhancement) of the pre-peak from ≈ 2 to $\approx 2.4\,\text{Å}^{-1}$ and a decrease in the peak intensity at $3.1\,\text{Å}^{-1}$. Also, above 7 kbar the peak around $5\,\text{Å}^{-1}$ splits into two broad but distinct peaks, at $\approx 4.5\,\text{Å}^{-1}$ and

$\approx 5.5\,\text{Å}^{-1}$ respectively. The evolution of these features is consistent with recent experimental observations by Mariedahl *et al.* [11], increasing our confidence in the ability of TIP4P/Ice to faithfully describe the structural properties of deep supercooled water.

COMPARISON WITH EXPERIMENTAL DATA

To obtain amorphous states that could be compared with the experimental glasses as shown in Fig. 3 of main text, the IS were annealed to 80 K and relaxed to ambient pressure. The annealing was carried out over an interval of 200 ps, and we used the Berendsen algorithm [12] for both temperature and pressure coupling with short relaxation times, respectively 0.8 and 1.8 ps. Here we adopted these algorithms to avoid artificial oscillations in T and P which are sometimes observed with other thermostats and barostats after abrupt changes in thermodynamic conditions. The Berendsen algorithm is known to provide the correct thermodynamics and structural averages, but incorrect fluctuations.

As explained in main text, the glass structures thus obtained are still not ready to be compared with experimental data; at such low temperatures quantum effects become relevant [13] and a correction, accounting for the delocalization of O atoms, has to be applied to the numerical results from the classical TIP4P/Ice potential. Fig. 3 shows the comparison of numerical and experimental data, after the numerical $g(r)$ has been convoluted with a Gaussian of variance $7.1 \times 10^{-3}\,\text{Å}^2$ as discussed in the main article; in Fig. S8 we compare the $g(r)$ before and after such correction is applied, for the glasses recovered at three different values of density. As expected, the convolution affects only the region of the first peak, while the correlations at larger separations are unaffected (although the curve is obviously smoothened).

HYDROGEN BONDS

To perform an accurate analysis based on topological properties it is of fundamental importance to correctly identify HBs at all thermodynamic conditions. Several different definitions of HB have been proposed throughout the years [14].

The definition of Luzar and Chandler [15] (LC) ($r_{\text{OO}} < 3.5\,\text{Å}$ and $\theta < 30^\circ$ where θ is the (smallest) $\text{H}\hat{\text{O}}\cdots\text{O}$ angle) when applied to the IS allows us to identify HBs with high

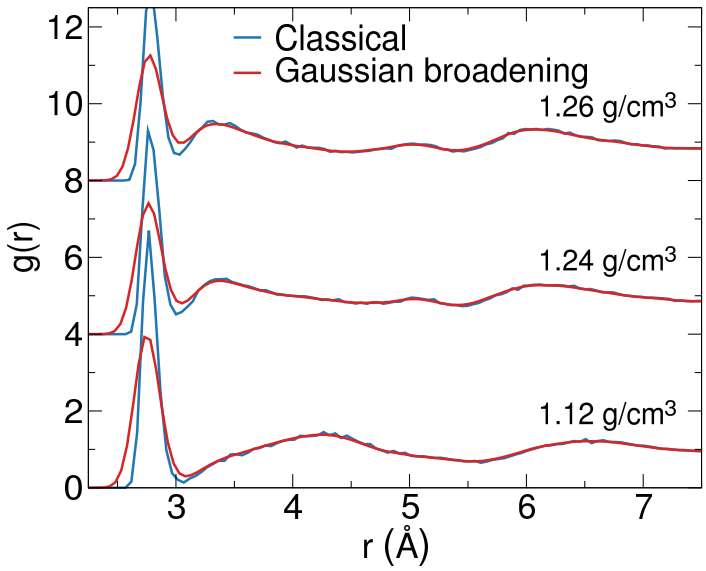

FIG. S8. Comparison of numerical $g(r)$ before and after application of quantum broadening corrections, for amorphous configurations at three different densities.

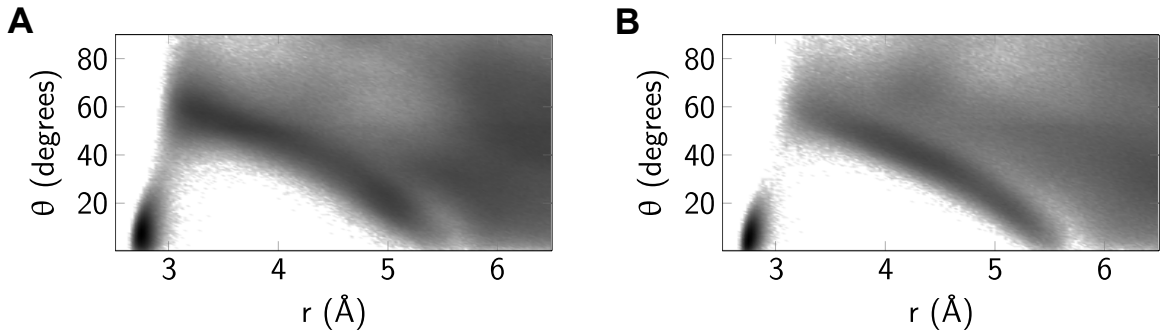

FIG. S9. Spatial density function, $g(r, \theta)$, of the OO distance r and the HÔ···O angle θ at (a) 13 kbar and (b) 2.5 kbar. The value of $g(r, \theta)$ is represented by intensity in logarithmic scale, increasing from white to black.

accuracy, despite the increasing distortion in the local environments that is observed upon isothermal compression. Figure S9 depicts the $g(r, \theta)$ distribution of the system at 2.5 and 13 kbar. With increasing pressure, the identification of HBs provided by the LC definition becomes less accurate since the distribution around the main HB peak ($r \approx 2.8$ Å, $\theta \approx 5°$) becomes broader. It should be noticed, however, that point density in Fig. S9 is shown in log scale, so that low-probability regions in $r - \theta$ space are accentuated with respect to high-probability ones.

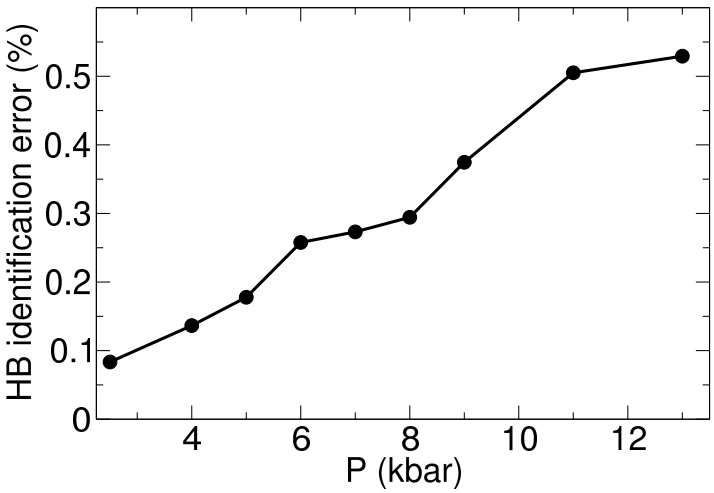

FIG. S10. Average identification error of HBs as a function of pressure with the Luzar-Chandler definition.

The average identification error committed by adopting the LC definition can be estimated as follows. We can consider "proper" HBs those that satisfy the LC conditions, and "uncertain" HBs those with a bond length $r < 3.5\,\text{Å}$ but with an angle within 20% above the LC angular threshold: $30° < \theta < 36°$. It appears likely that at least a fraction of these uncertain bonds should be considered as proper HBs. The error can then be defined as the ratio between the number of uncertain and proper HBs. The results are reported in Fig. S10, showing that the average error is below 1% even at the highest pressure. The LC definition of HB is therefore reasonably valid over the whole isotherm.

To investigate an alternative definition, instead of using the LC angular threshold $\theta^* = 30°$, we choose a r-dependent angular threshold $\theta^* = \theta^*(r)$ with the aim of minimizing the error intrinsic in the definition. The simplest approach uses a linear dependence, $\theta^*(r) = \theta_0 + \alpha r$. We thus identify a potential of mean force PMF (per unit thermal energy)

$$\text{PMF} = -\ln g(r, \theta) \tag{S1}$$

and obtain the values of θ_0 and α by identifying the linear path of maximum PMF passing through the saddle point at $r \approx 3\,\text{Å}$ and $\theta \approx 35°$. This path identifies the optimal boundary between H-bonded and non-H-bonded pairs. By optimising over the data at $P = 13\,\text{kbar}$, we find:

$$\theta_0 \approx 113°, \qquad \alpha \approx -26\,°\,\text{Å}^{-1}. \tag{S2}$$

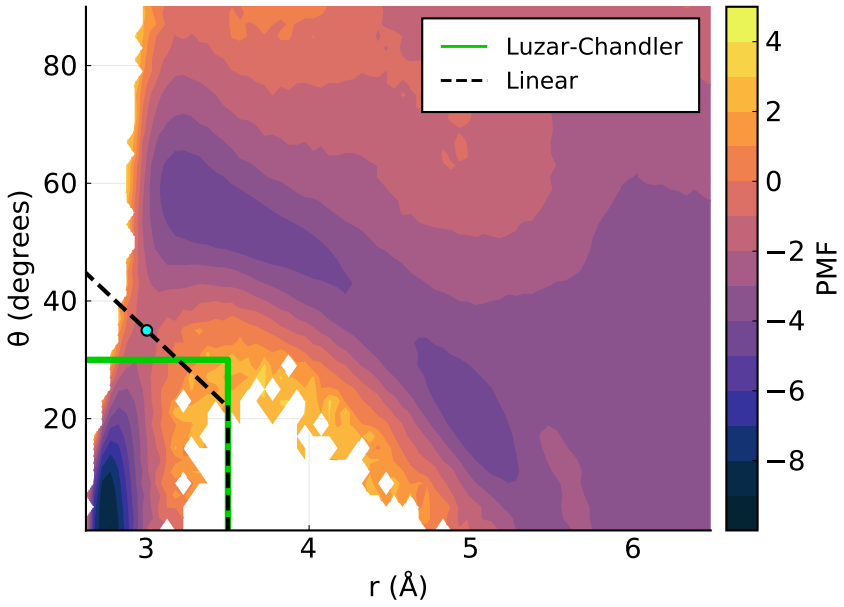

FIG. S11. Comparison, at $P = 13\,\mathrm{kbar}$, of the Luzar-Chandler definition of HB and the new definition obtained by evaluating the linear path ($\theta = \theta_0 + \alpha r$) of maximum PMF through the saddle point (cyan circle, found approximately at $r \approx 3\,\text{Å}$ and $\theta \approx 35°$).

With this method, two molecules are H-bonded if their O−O distance is $r < 3.5\,\text{Å}$ and their HÔ···O angle satisfies $\theta < 113° - 26\,°\,\text{Å}^{-1} r$. See Fig. S11. At $P = 13\,\mathrm{kbar}$, where the difference between the two definitions is largest, the new definition counts an average of ≈ 2002 H-bonded pairs out of 1000 molecules, whereas the LC criterion identifies ≈ 1995 pairs; that is, an average difference of 7 HBs per configuration. As the pressure is decreased, the difference between the two definitions decreases. Given the minute difference, we conclude that even in this high-P regime, the LC definition can be adopted without the risk of significantly compromising the topological description of the system. Hydrogen bonds in the following (and in the main text) are thus always identified according to the LC definition in the IS.

NETWORK DEFECTS

In the explored thermodynamic range, we observe molecules with coordination numbers 3 or 5 (network defects); Following the nomenclature introduced by Saito *et al.* [16], 5-coordinated defects donate 2 HBs and accept 3 (H^2O^3), while 3-coordinated defects can either donate 2 HBs and accept 1 (H^2O^1) or donate 1 and accept 2 (H^1O^2). In a previous

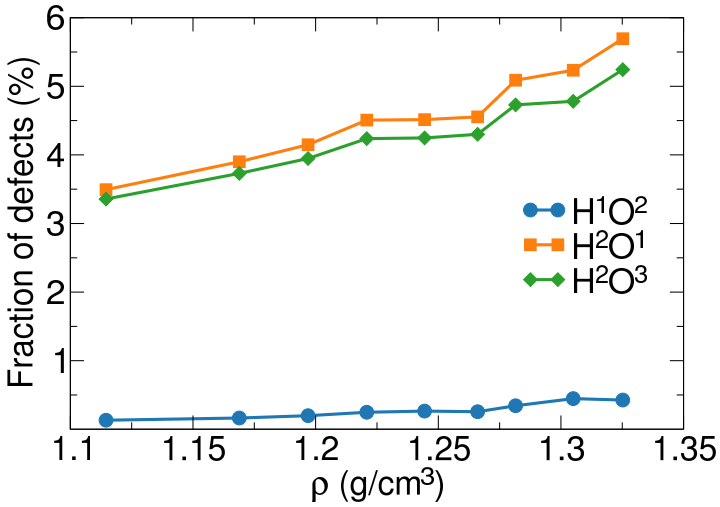

FIG. S12. Population of network defects as a function of density.

work [8] we have shown that network defects appear to have a role in the structural transformations that characterize the liquid-liquid phase transition of (TIP4P/Ice) water; along the 188 K isotherm, from ambient pressure up to 2.5 kbar, H^2O^1 and H^2O^3 were found to be almost-perfectly paired, thus conserving the total number of HBs and imposing only a minor energetic cost on the system; the presence of H^1O^2, a geometry that sacrifices a HB, was negligible.

The fraction of defects, distinguished by species, that we observed along the 188 K isotherm from 2.5 to 13 kbar is shown in Fig. S12. At all pressures, more than 99.5% of the H atoms are involved in HBs, indicating that, despite the high pressure and intense structural distortion, practically all molecules donate two hydrogens for bonding. While most molecules still participate in four HBs, there is a fraction of network defects, accepting either one or three bonds, whose concentration increases (roughly) linearly with density. The strong correlation between the number of five- and three-coordinated molecules and the density might suggest that the primary effect of compression is to convert a pair of tetrahedrally-coordinated molecules into a H^2O^1 – H^2O^3 defect pair. Consistent with the weak dependence of E on ρ (see Fig. 1 of the main text), such a transformation does not have a significant energetic cost, preserving the total number of HBs while improving the packing.

The structural properties of network defects in this thermodynamic regime are also consistent with the observations made in Ref. [8]. Figure S13 shows the contribution to the $g(r)$

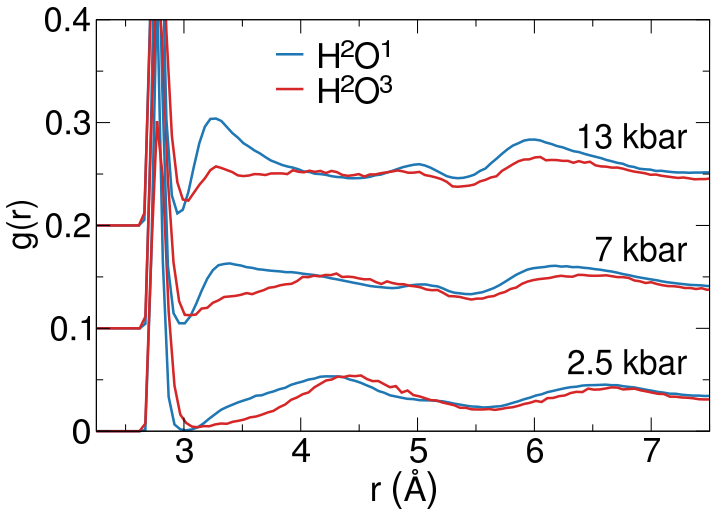

FIG. S13. Contribution of network defects to $g(r)$ evaluated in the IS at three different pressures along the 188 K isotherm. Curves were shifted by 0.1 along the vertical axis; the $r \to \infty$ limit indicates the relative concentration of the associated defect species.

from network defects at three different pressures; the two curves represent the radial structure around H^2O^1 and H^2O^3 molecules, respectively. It is therefore clear that 3-coordinated molecules participate actively in the interpenetration phenomenon, while 5-coordinated ones display an increasingly featureless distribution as P increases.

TOPOLOGY AND STRUCTURE

The core results about the structure of the system are obtained by classifying the pairs of molecules in the system according to their chemical distance and ring length, as outlined in the main text. The definition of ring that we adopted here is the same that we proposed in Ref. [8]. For a given pair of molecules (i, j) at chemical distance D, the ring length L associated to this pair is the length (measured in steps along the HB network) of the closed path obtained by joining the two shortest non-intersecting HB-paths between i and j. By definition, $L \geq 2D$.

With this approach, we first separate all pairs of molecules in the system depending on their chemical distances D, so as to evaluate the contribution to the radial distribution

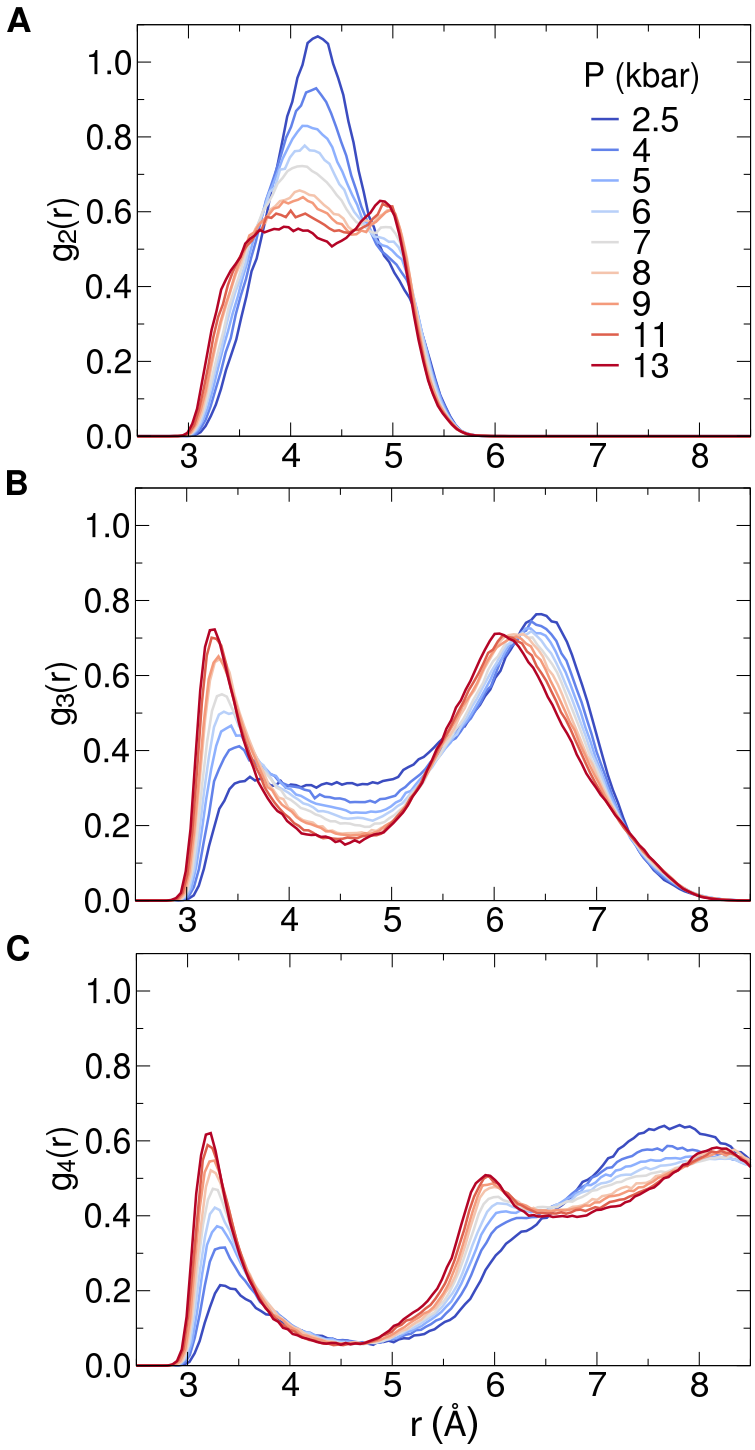

FIG. S14. Contributions to the $g(r)$ along the 188 K isotherm separated by coordination shells: (a) $D = 2$, (b) $D = 3$, (c) $D = 4$. Pressure increases from blue to red.

function $g(r)$ arising from pairs at chemical distance D, such that

$$g(r) = \sum_D g_D(r).$$

The results of this decomposition at pressures 2.5 and 13 kbar are shown in Fig. 4 of the main text; here, in Fig. S14 we report the complete pressure dependence of the g_D contributions (for $D = 2, 3, 4$) along the 188 K isotherm.

As a second step, each pair of molecules at chemical distance D is further characterized in terms of its ring length L; the total structure of the system is now decomposed in such a way that

$$g(r) = \sum_D \sum_L g_D^L(r).$$

Fig. S15 shows a sample HB network, where two different pairs of molecules are highlighted, in blue and red respectively. The ring length associated to the blue pair (a) is $L = 6$, and that associated to the read pair (b) is $L = 8$; the two pairs are characterized by different ring lengths, despite the fact that the blue molecules are included in the ring that connects the red pair.

The pressure dependence of each g_D^L along the isotherm is shown in Figs. S16–S18. The behavior of g_2 and g_4 (and their components g_2^L and g_4^L) is extensively discussed in the main text. Besides the increase in the interstitial peak, g_3 does not show clear relevant features in the evolution from high to very-high densities. As seen in Fig. S17, the (small) increase in the g_3 contribution at $r \approx 6$ Å can be ascribed fundamentally to the g_3^8 component, where a peak continuously shifting from ≈ 6.5 Å to ≈ 6 Å is observed, without evidence of significant transformations in the underlying network structure.

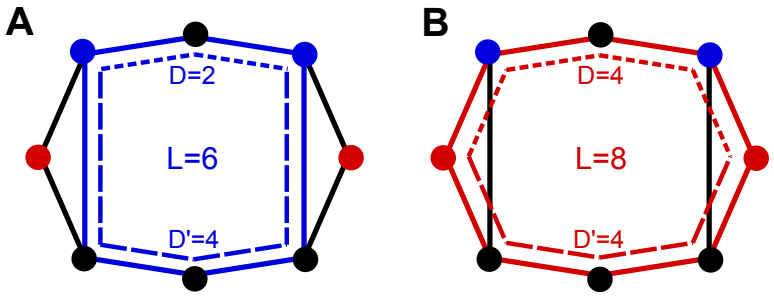

FIG. S15. Sample schematics of a HB network showing how rings and ring lengths are identified. (a) The blue molecules are at chemical distance $D = 2$ (short-dashed path), and the second-shortest path (long-dashed) has length $D' = 4$; by joining these two paths we obtain a ring of length $L = 6$. (b) The two shortest paths between the pair of red molecules are both of length 4, producing a ring of length $L = 8$.

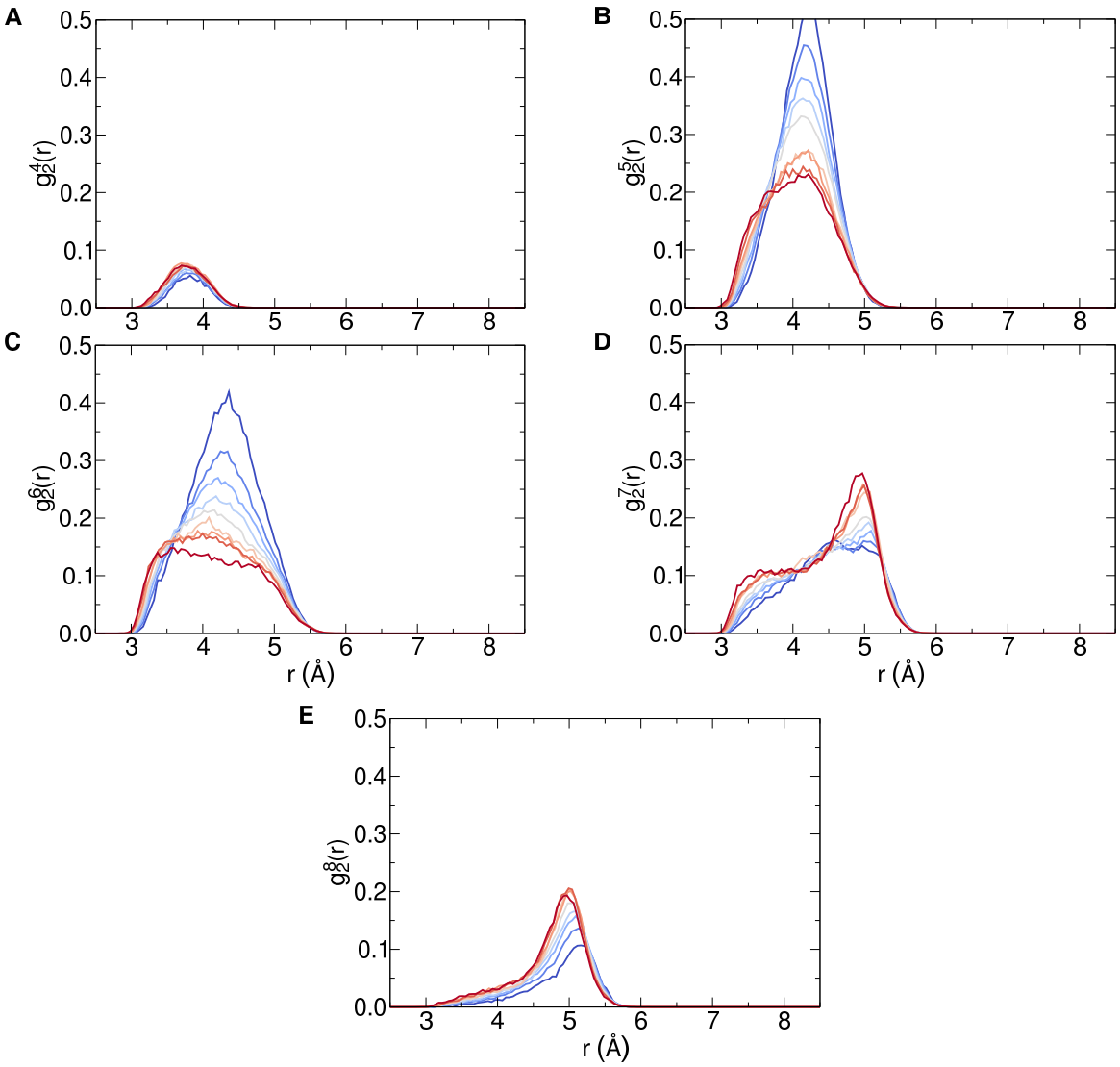

FIG. S16. Contributions to the $g(r)$ arising from pairs of molecules at chemical distance $D = 2$ in rings of length L ranging from (a) $L = 4$ to (e) $L = 8$. Pressure increases from blue to red.

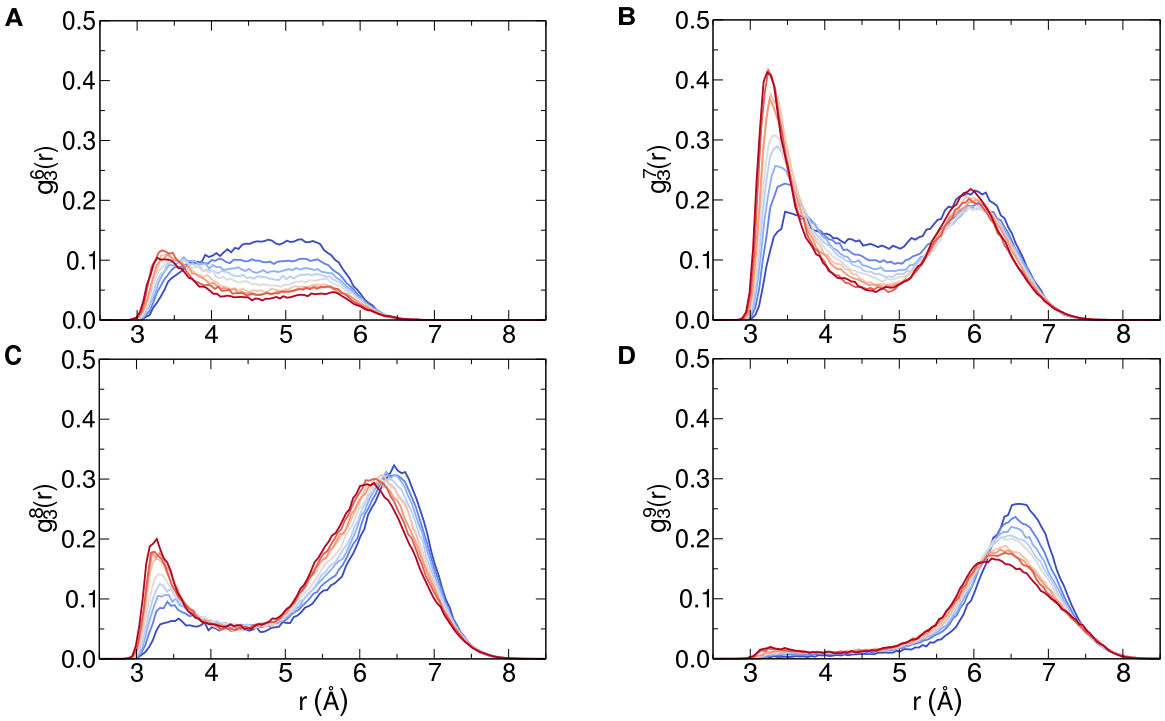

FIG. S17. Contributions to the $g(r)$ arising from pairs of molecules at chemical distance $D = 3$ in rings of length L ranging from (a) $L = 6$ to (d) $L = 9$. Pressure increases from blue to red.

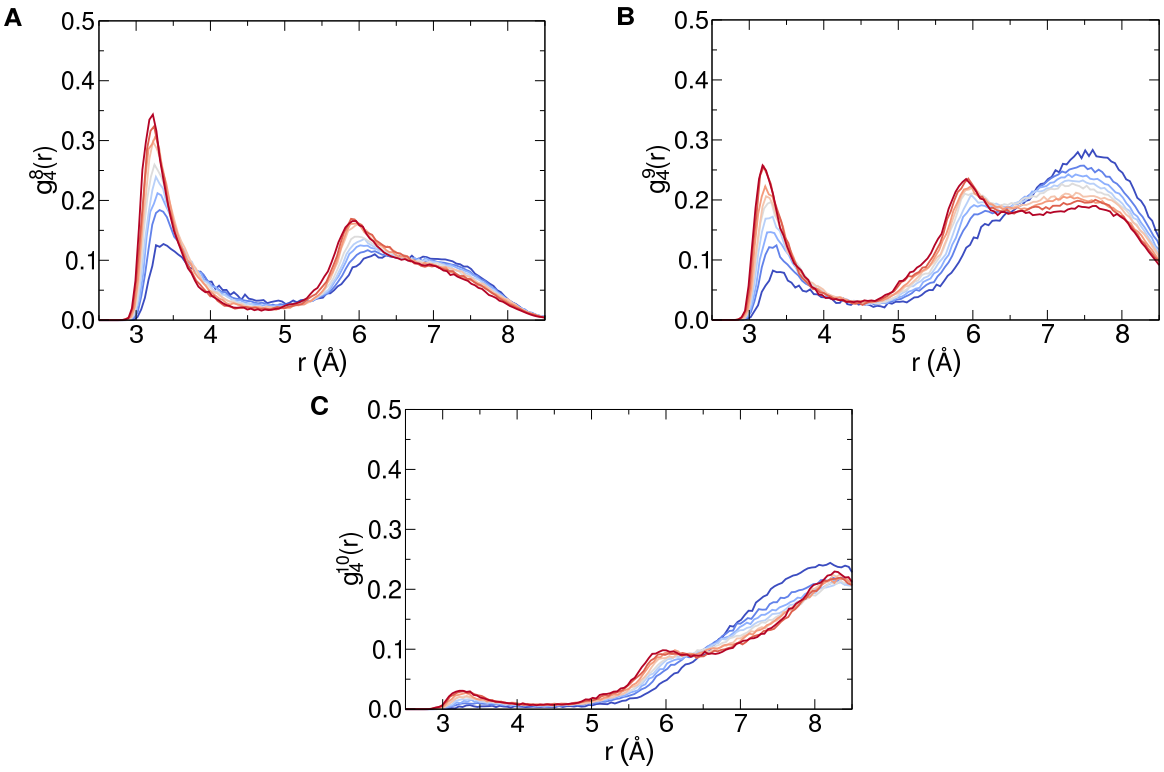

FIG. S18. Contributions to the $g(r)$ arising from pairs of molecules at chemical distance $D = 4$ in rings of length L ranging from (a) $L = 8$ to (c) $L = 10$. Pressure increases from blue to red.

[1] J. L. F. Abascal, E. Sanz, R. García Fernández, and C. Vega, J. Chem. Phys. **122**, 234511 (2005).

[2] M. J. Abraham, T. Murtola, R. Schulz, S. Páll, J. C. Smith, B. Hess, and E. Lindahl, SoftwareX **1-2**, 19 (2015).

[3] D. Frenkel and B. Smit, *Understanding Molecular Simulation from Algorithms to Applications* (Academic Press, San Diego, 2002).

[4] M. Parrinello and A. Rahman, J. Appl. Phys. **52**, 7182 (1981).

[5] B. Hess, H. Bekker, H. J. Berendsen, and J. G. Fraaije, J. Comput. Chem **18**, 1463 (1997).

[6] M. P. Allen and D. J. Tildesley, *Computer Simulation of Liquids*, second edition ed. (Oxford University Press, Oxford, 2017).

[7] P. G. Debenedetti, F. Sciortino, and G. H. Zerze, Science **369**, 289 (2020).

[8] R. Foffi, J. Russo, and F. Sciortino, J. Chem. Phys. **154**, 184506 (2021).

[9] F. H. Stillinger, *Energy Landscapes, Inherent Structures, and Condensed-Matter Phenomena* (Princeton University Press, Princeton, New Jersey, 2015).

[10] J.-P. Hansen and I. R. McDonald, *Theory of Simple Liquids: With Applications of Soft Matter* (Elsevier, Academic Press, Amsterdam, 2013).

[11] D. Mariedahl, F. Perakis, A. Späh, H. Pathak, K. H. Kim, G. Camisasca, D. Schlesinger, C. Benmore, L. G. M. Pettersson, A. Nilsson, and K. Amann-Winkel, J. Phys. Chem. B **122**, 7616 (2018).

[12] H. J. C. Berendsen, J. P. M. Postma, W. F. van Gunsteren, A. DiNola, and J. R. Haak, J. Chem. Phys. **81**, 3684 (1984).

[13] C. P. Herrero and R. Ramírez, J. Chem. Phys. **137**, 104505 (2012).

[14] R. Kumar, J. R. Schmidt, and J. L. Skinner, J. Chem. Phys. **126**, 204107 (2007).

[15] A. Luzar and D. Chandler, Nature **379**, 55 (1996).

[16] S. Saito, B. Bagchi, and I. Ohmine, J. Chem. Phys. **149**, 124504 (2018).